

# CHALMERS



## Numerical investigation of the flow in a swirl generator, using OpenFOAM

*Master's Thesis in Fluid Mechanics*

OSCAR BERGMAN

Department of Applied Mechanics  
*Division of Fluid Mechanics*  
CHALMERS UNIVERSITY OF TECHNOLOGY  
Göteborg, Sweden 2010  
Master's Thesis 2010:25



Numerical investigation of the flow in a swirl generator,  
using OpenFOAM

Master's Thesis in Fluid Mechanics  
OSCAR BERGMAN

Department of Applied Mechanics  
*Division of Fluid Mechanics*  
CHALMERS UNIVERSITY OF TECHNOLOGY  
Göteborg, Sweden 2010

Numerical investigation of the flow in a swirl generator, using OpenFOAM  
OSCAR BERGMAN

©OSCAR BERGMAN, 2010

Master's Thesis 2010:25  
ISSN 1652-8557  
Department of Applied Mechanics  
Division of Fluid Mechanics  
Chalmers University of Technology  
SE-412 96 Göteborg  
Sweden  
Telephone: + 46 (0)31-772 1000

Chalmers Reproservice  
Göteborg, Sweden 2010

## Abstract

This work presents results from OpenFOAM simulations conducted on a swirl generator designed to give similar flow conditions to those of a Francis turbine operating at partial load. Francis turbines are one of the most commonly used water turbines. In these turbines, there is however a frequent problem occurring at part load. Due to a swirling flow in the draft tube, a transient helical vortex rope builds up and creates severe pressure fluctuations in the system that increase the risk for fatigue. To predict and control such flow features is therefore critical. A test rig was developed at the "Politehnica" University of Timisoara, Romania, to provide a detailed experimental database of such flow features. This test rig has four parts: leaning strout vanes, stay vanes, a rotating runner which is designed to have zero torque, and a convergent divergent draft tube.

In this work, numerical results are compared and validated against measurements realized on the swirling flow test rig at the Polytechnica University of Timisoara in Romania. The computational mesh is created with ICEM-Hexa and the parts have been meshed separately and then merged together, using General Grid Interfaces (GGI) to couple them numerically. The finite volume method is used to solve both the unsteady and steady state Reynolds Averaged Navier Stokes equations and the standard  $k-\varepsilon$  model is used to close the turbulence equations. Steady-state simulations is a preliminary method, which is less time-consuming and predicts the general behavior of the flow field. It also provides good initial conditions for the unsteady simulations. For the unsteady simulations, the mesh of the rotating part of the domain is rotating and the coupling between the stationary and rotating parts is handled by a sliding GGI interface.

The simulation results shows a developing vortex rope in the draft tube which gives rise to oscillations of flow properties in the system. The size and shape of this vortex rope, as well as the frequency of the oscillations it gives rise to, is highly dependent on the rotational speed of the free runner. The results show that a rotational speed of 920 rpm on the runner, corresponds best with the measurements out of the three rotational speeds 870 rpm, 890 rpm and 920 rpm. The rotational speed of 870 rpm gives a positive moment on the runner, an rpm of 890 of almost zero moment, and a speed of 920 rpm gives a positive moment on the runner. Fourier analysis of the pressure fluctuations show that several new frequencies has been introduced compared to a previous OpenFOAM study which was only made on the draft tube. The main frequencies for a rotational speed of 920 rpm have been estimated to 3.0 Hz corresponding to an extraction/retraction of the vortex rope, 18.02 Hz which comes from the rotation of the vortex rope and 153.19 Hz which is caused by the rotor stator interaction. Furthermore, the amplitudes of the fourier spectra have shown good agreement with the previous study.



# Contents

<b>Abstract</b>	<b>I</b>
<b>Preface</b>	<b>V</b>
<b>Aknowledgements</b>	<b>V</b>
<b>1 Introduction</b>	<b>1</b>
1.1 Experimental rig . . . . .	2
1.2 Measurements . . . . .	3
1.3 Previous studies . . . . .	3
<b>2 Theory</b>	<b>5</b>
2.1 Governing Equations . . . . .	5
2.1.1 Reynolds-Averaged Navier-Stokes equations (RANS) . . . . .	5
2.1.2 Eddy viscosity models . . . . .	6
2.1.3 $k - \varepsilon$ turbulence model . . . . .	6
2.2 Computational Fluid Dynamics . . . . .	7
<b>3 Method</b>	<b>8</b>
3.1 Description of the OpenFOAM CFD toolbox . . . . .	8
3.2 Numerical Setup . . . . .	9
3.2.1 Steady-State simulations . . . . .	9
3.2.2 Unsteady Simulations . . . . .	10
<b>4 Results and Discussion</b>	<b>10</b>
4.1 Steady-State Simulations . . . . .	10
4.1.1 Comparison with theoretical design profiles . . . . .	11
4.1.2 Comparison with LDV measurements . . . . .	12
4.1.3 Comparing moment forces . . . . .	14
4.2 Unsteady Simulations . . . . .	15
4.2.1 Comparison with theoretical design profiles . . . . .	15
4.2.2 Comparison with LDV measurements . . . . .	16
4.2.3 Comparison between the PISO based solver and a SIMPLE based solver . . . . .	18
4.2.4 Comparison of moment forces and pressure fluctuations . . . . .	19
4.3 Fourier Analysis . . . . .	22
4.3.1 Fourier analysis theory . . . . .	22
4.3.2 Fourier algorithm in Matlab . . . . .	23
4.3.3 Results of fourier analysis . . . . .	24
<b>5 Conclusion</b>	<b>27</b>
<b>6 Future work</b>	<b>27</b>





# Preface

In this study the swirling flow of a swirl generator has been analyzed and numerically investigated. The OpenFOAM software has been tested and validated against experiments. The work has been carried out from January 2010 to June 2010 at the Department of Applied Mechanics Division of Fluid Mechanics Chalmers University of Technology, Sweden, with Oscar Bergman as student and with Olivier Petit and Professor Håkan Nilsson from the department of Applied Mechanics as supervisors.

## Acknowledgements

I would like to acknowledge the Timisoara research group, Professor Romeo F.Susan-Resiga, Sebastian Muntean, Alan Bosioc and their team for sharing experimental results with me. I would also like to acknowledge the Swedish National Infrastructure for Computing (SNIC) and Chalmers Center for Computational Science and Engineering (C3SE) for providing computer resources. I would like to give my thanks to Andreo Gonzalez, Shasha Xie, Xin Zhao and everyone else at the department of Applied Mechanics for creating a nice working atmosphere. Also I would like to thank my girlfriend Elin Holstensson and my parents Ove and Elisabeth Bergman for all love, patience and support. Finally I want to thank my supervisors Håkan Nilsson and Olivier Petit for being very patient and for sharing their knowledge. They really made this project a stimulating and fun learning experience.

Göteborg, April 2010  
Oscar Bergman



# 1 Introduction

Sweden has a good access to water power. With the Norwegian mountains in the north-west, the rivers through Sweden provide the way for the water to reach Östersjön. During spring, the snow melts on the mountaintops and the water finds its way to the surface of the ocean. Almost all electric energy in Sweden is supplied by water power and nuclear power. These days however, when a lot of resources are put to alternative energy sources, water turbines are often turned on and off and used for filling in when the energy demand is high. Wind power is for example sensitive to weather, and can often fail to deliver the power quota which it is set to provide, thus creating a gap in the electric grid. During the conditions of starting and stopping the water turbines, an unwanted phenomenon occurs. Some of the water turbines used today are Francis turbines. They are radial and mixed flow turbines. When these turbines operate at partial load, the flow in the draft tube gets a swirling flow profile. This is due to the fact that the runner is designed to neutralize the swirl created by the guide vanes at the best efficiency point. If the turbine is operating away from the efficiency point, this swirl will not be neutralized to the same extent. This may then cause a transient helical vortex rope to build up and create pressure fluctuations which greatly increases the risk of fatigue damage on the turbines. Solving this problem is crucial, and knowing more about the flow features of a swirling flow will help development of techniques that can prevent these problems to occur.

This work presents numerical investigations of a swirl generator test rig installed at the Polytechnica University of Timisoara, Romania. The swirl generator is designed to give similar flow features to that of a Francis turbine operating at part load. That is, at certain flow discharge, a vortex rope builds up and creates pressure fluctuations which affects the stresses on the runner. The swirl generator consists of strout blades, stayvanes, a free runner and a convergent divergent draft tube.



*Figure 1.1: A precessing vortex rope, created by the swirling flow in the test rig.*

Figure 1.1 shows the phenomenon which is studied in this work. A precessing helical vortex rope caused by the flow conditions created in the swirl generator.

## 1.1 Experimental rig

The swirl generator is shown in Figure 1.2. It consists of four parts: a strout, a free runner with 10 blades, 13 guide vanes and a draft tube with a swirlcone nozzle. The inlet is located at the strout section of Figure 1.2 and shown as an arrow in the figure. The purpose of the free rotating runner is just to redistribute the total pressure to obtain a more similar distribution to that of a Francis turbine at partial discharge. The experimental rig is built with a draft tube in plexiglass in order to better visualize the flow, as well as to enable velocity measurements with LDV at the three windows seen to the left in Figure 1.2.

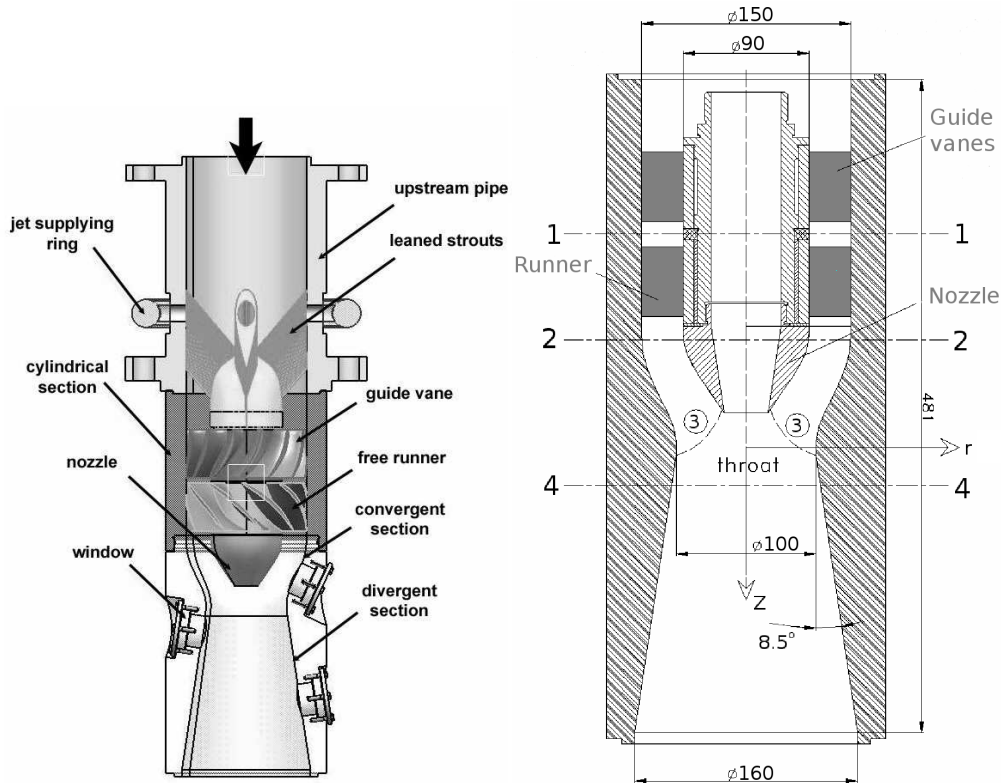


Figure 1.2: General sketch of the swirlgenerator test rig (left) and the dimensions and cross-sections (right).

The leaning strout blades seen to the left in Figure 1.2 holds up the stayvanes, runner and swirlcone. The guide vanes and the free runner have the purpose to direct the flow and create a swirling flow profile. The guide vanes produce a swirling flow that has almost constant total pressure and the runner then redistributes the total pressure by accumulating energy near the hub and thus acting like a turbine, and consume energy at the tip i.e. acting like a pump. This results in zero torque which enables the runner to rotate freely and redistribute the total pressure without changing the kinetic energy of the flow. The draft tube is a diffuser which purpose is to decelerate the flow coming from the runner and recover the static pressure. To the right of Figure 1.2, the dimensions of the swirl generator are shown. The z-axis is defined in the flow direction, and the origin is at the throat. The test rig has an inner hub radius of 45 mm and an inner case radius of 75 mm and its total axial length is 481 mm. Both guide vanes and runner have an axial length of 60 mm. The wall of the draft tube has an angle of  $8.5^\circ$  at the divergent section.

Measurements and simulation results are validated at cross-sections 1 and 2, against a

theoretical design model, which was used when designing the swirl generator. The cross-sections are seen in the right of Figure 1.2. Cross-section 1 is located between the stay vanes and the runner and cross-section 2 is located just downstream the runner. Cross-sections 3 and 4 are not used in this work.

## 1.2 Measurements

The LDV measurements were made at the Politehnica University of Timisoara and presented by Bosioc et al. [6]. They were made with two-component LDV and with  $10\ \mu\text{m}$  aluminium particles inserted into the flow to reflect the laser beams. The meridional and tangential velocity is then measured at the three survey axes shown on the left in Figure 1.3. The arrows indicates the start of the survey lines, that is, where  $x = 0$  in the plots. Survey axes 1 and 2 have the same angle to the radial axis as the draft tube wall has to the z-axis, which is  $8.5^\circ$ . Survey axis 0 has an angle of  $25^\circ$  to the radial axis. All measurements were made at a total flow discharge of 30 l/s, which corresponds to 80 % of the maximum power of the used pump.

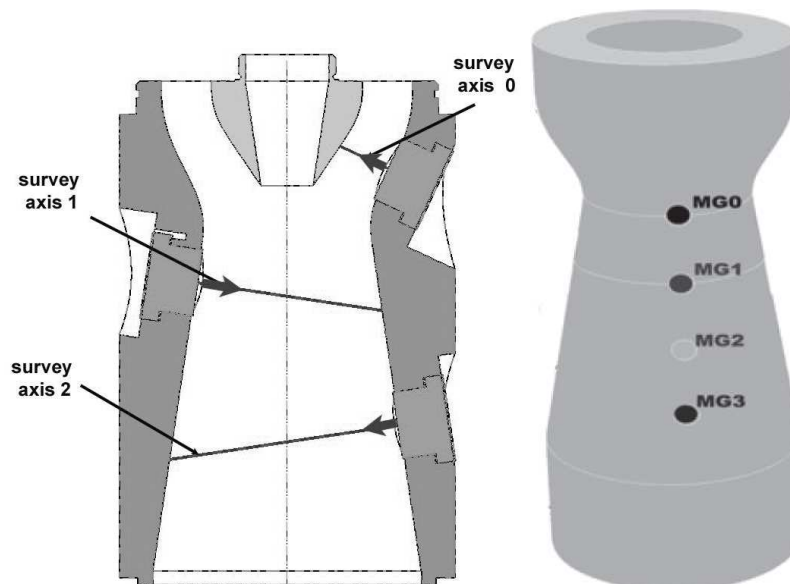


Figure 1.3: The three survey lines(left) and location of pressure transducers (right).

The unsteady static pressure is measured with pressure transducers at MG0, MG1, MG2 and MG3 which are located at 0, 50, 100, and 150 mm downstream the throat, seen to the right of Figure 1.3.

## 1.3 Previous studies

There have been many studies on swirling flows and on the problems caused by precessing vortices. One early study, made in year 2000, was the Flow Investigation in Draft Tubes (FLINDT) research project [2]. This study provided a large experimental database on the swirling flow phenomenons. Unfortunately, the FLINDT data is available only to the partners of that project. The complexity of these large scale experimental projects makes them difficult and costful to realize, which is why measurements of this type usually is made on smaller scaled models. The design of the swirl generator testrig in Timisoara has

similar goals to that of the FLINDT project. The optimal number of blades have been estimated for creating similar swirling profiles to that of Francis turbines at part load, and the dimensions of the stay vanes and runner blades have been designed using a quasi-3D inverse design method for turbomachinery blades [15] to create a precessing vortex rope [16]. The convergent divergent draft tube have been designed with a beneficial shape for swirling flows [5] and 2D Laser Doppler Velometry measurements have been made for investigating the flow at different parts of the swirl generator. Resiga [17] introduced a technique to control the instabilities by using axial jet control in the discharge cone. In later studies [10], it was shown that at a jet discharge corresponding to 10% of the total turbine discharge neutralizes the pressure oscillations the most. Muntean and Resiga later confirmed this in a 3D unsteady numerical investigation [4]. Using this technique would however require a to large fraction of the discharging flow to be bypassed, so Resiga and Muntean later showed that such a jet control can instead be obtained by using a flow feedback method downstream the cone [14]. In a study by Muntean et al. [11], only the draft tube was used when simulating the unsteady flow in 3D. Petit [13] extended the studies by including all parts of the swirl generator test rig, which makes the draft tube inlet conditions different from those applied by Muntean et al. [11]. This project aims at creating a database of simulation results which can be used for further studies in attempts to solve this problem.

## 2 Theory

When numerically simulating a flow field, the techniques and methods for this can be of many different kinds. The most used technique is based on the finite volume method which uses small control volumes to discretise the governing differential equations.

### 2.1 Governing Equations

The equations that describe a fluid in motion are derived from the conservation of mass, momentum and energy. The motion of an incompressible fluid is described by the Navier-Stokes equations, which state that changes in momentum of a fluid only depends on the surrounding pressure and the internal viscous forces acting on the fluid:

$$\underbrace{\rho \left( \frac{\partial u_i}{\partial t} + v_j \frac{\partial u_i}{\partial x_j} \right)}_{\rho \frac{Du_i}{Dt}} = -\frac{\partial p}{\partial x_i} + \frac{\partial}{\partial x_j} \left( \mu \left( \frac{\partial u_i}{\partial x_j} + \frac{\partial u_j}{\partial x_i} \right) \right) + \rho f_i \quad (2.1)$$

Where  $\rho$  is the density,  $\frac{D}{Dt}$  the material derivative,  $u$  is the velocity,  $t$  is time,  $p$  is the static pressure,  $\mu$  is the dynamic viscosity and  $f$  is the body force acting on the fluid. Body forces can be for example gravity, centrifugal or Coriolis forces.

The Navier-Stokes equations are complemented with the continuity equations, which is a statement of conservation of mass:

$$\frac{\partial \rho}{\partial t} + \frac{\partial \rho u_j}{\partial x_j} = 0 \quad (2.2)$$

Dealing with water, this equations can be simplified due to the assumption of incompressibility, which means that density is independent of the pressure, and so the continuity equation becomes:

$$\frac{\partial u_j}{\partial x_j} = 0 \quad (2.3)$$

Inserting into the Navier-Stokes equations we get:

$$\rho \left( \frac{\partial u_i}{\partial t} + v_j \frac{\partial u_i}{\partial x_j} \right) = -\frac{\partial p}{\partial x_i} + \mu \frac{\partial^2 u_i}{\partial x_j^2} + \rho f_i \quad (2.4)$$

where the first term from the left is the unsteady term, the second term is the convection term. The sum of these two represents the inertia of the fluid. The third is the pressure gradient, the fourth is the viscosity term, and the last is again body forces acting on the fluid. Body forces like centrifugal or Coriolis forces appear when solving the equations in a rotating frame of reference.

#### 2.1.1 Reynolds-Averaged Navier-Stokes equations (RANS)

The Reynolds-Averaged Navier-Stokes equations are the time averaged equations of the Navier-Stokes equations. They are obtained by decomposing the instantaneous velocity vectors into one averaged part and one fluctuation part, i.e.

$$u(\mathbf{x}, \mathbf{t}) = \bar{U}(x) + u'(\mathbf{x}, \mathbf{t}) \quad (2.5)$$

inserting into the Navier-Stokes equations and time averaging yields :

$$\rho \frac{\partial \bar{U}_j \bar{U}_i}{\partial x_j} = \rho \bar{f}_i + \frac{\partial}{\partial x_j} \left[ -\bar{P} \delta_{ij} + \mu \left( \frac{\partial \bar{U}_i}{\partial x_j} + \frac{\partial \bar{U}_j}{\partial x_i} \right) - \overline{\rho u'_i u'_j} \right] \quad (2.6)$$

In the unsteady RANS equations, an additional time dependant term is added on the left hand side:  $\rho \frac{\partial \bar{U}_i}{\partial t}$ .

As this averaging is performed, the new term  $\overline{u'_i u'_j}$  appears. This is the Reynolds stress tensor. It is an additional symmetric stress tensor that is added due to turbulence and which represents the correlations between fluctuating velocities. This stress tensor is unknown and it makes the system of equations unsolvable, as we have more unknowns than equations. The equations can then be closed using a turbulence model for the Reynolds stresses.

### 2.1.2 Eddy viscosity models

In eddy viscosity models, the closure problem is solved by introducing a linkage between the Reynolds stresses and the velocity gradients, using an eddy viscosity  $\mu_t$ . The diffusion term then becomes:

$$\frac{\partial}{\partial x_j} \left[ \mu \left( \frac{\partial \bar{U}_i}{\partial x_j} + \frac{\partial \bar{U}_j}{\partial x_i} \right) - \rho \overline{u'_i u'_j} \right] = \frac{\partial}{\partial x_j} \left[ (\mu + \mu_t) \left( \frac{\partial \bar{U}_i}{\partial x_j} + \frac{\partial \bar{U}_j}{\partial x_i} \right) \right] \quad (2.7)$$

which gives us

$$\overline{\rho u'_i u'_j} = -\mu_t \left( \frac{\partial \bar{U}_i}{\partial x_j} + \frac{\partial \bar{U}_j}{\partial x_i} \right) \quad (2.8)$$

if we set  $i=j$ , the reynolds stress becomes

$$\overline{u'_i u'_j} \equiv 2k \quad (2.9)$$

where  $k$  is the turbulent kinetic energy. Setting  $i=j$  however, the continuity equation would imply that  $\overline{u'_i u'_j} = 0$ . So in order to set  $i=j$ , we need to add  $2/3 \rho \delta_{i,j} k$  to the equation, i.e.

$$\overline{u'_i u'_j} = -\mu_t \left( \frac{\partial \bar{U}_i}{\partial x_j} + \frac{\partial \bar{U}_j}{\partial x_i} \right) + \frac{2}{3} \rho \delta_{i,j} k \quad (2.10)$$

This relation is called the *Boussinesq Assumption* and the idea of this is to model the small-scale eddies with a viscosity term, similar to the way the momentum friction forces in a fluid are modeled with a molecular viscosity.

### 2.1.3 $k - \varepsilon$ turbulence model

The  $k - \varepsilon$  turbulence model is a two-equation eddy viscosity model that uses two transport equations to represent the turbulent properties of the flow. The equation of turbulent kinetic energy is derived from the Navier-Stokes equation. It includes convection terms, production terms, turbulent diffusion terms and dissipation. The turbulent dissipation term  $\varepsilon$ , represents the transformation of kinetic energy at smaller scales into internal energy. However, there are many unknowns in the  $k$ -equation, dissipation being one amongst them. And so the  $k$ -equation is complemented with the dissipation-equation.

Turbulent kinetic energy-equation:

$$\frac{\partial(\rho k)}{\partial t} + \frac{\partial \rho k U_j}{\partial x_j} = \frac{\partial}{\partial x_j} \left[ \left( \mu + \frac{\mu_t}{\sigma_k} \right) \frac{\partial k}{\partial x_j} \right] + P_k - \rho \varepsilon \quad (2.11)$$

Dissipation -equation:

$$\frac{\partial(\rho \varepsilon)}{\partial t} + \frac{\partial(\rho \varepsilon U_j)}{\partial x_j} = \frac{\partial}{\partial x_j} \left[ \left( \mu + \frac{\mu_t}{\sigma_\varepsilon} \right) \frac{\partial \varepsilon}{\partial x_j} \right] + C_{1\varepsilon} \frac{\varepsilon}{k} P_k - C_{2\varepsilon} \rho \frac{\varepsilon^2}{k} \quad (2.12)$$



$$\mu_t = \rho C_\mu \frac{k^2}{\varepsilon}, \quad P_k = -\overline{\rho u_i' u_j'} \frac{\partial u_j}{\partial x_i} = \mu_t 2S_{ij} S_{ij}, \quad S_{ij} = \frac{1}{2} \left( \frac{\partial \bar{U}_i}{\partial x_j} + \frac{\partial \bar{U}_j}{\partial x_i} \right)$$

Here we have  $\mu_t$  as the eddy viscosity and  $P_k$  as the production of turbulent kinetic energy. The model constants are given by:

$$C_{1\varepsilon} = 1.44, \quad C_{2\varepsilon} = 1.92, \quad C_\mu = 0.09, \quad \sigma_k = 1.0, \quad \sigma_\varepsilon = 1.3$$

The k- $\varepsilon$  model uses wall functions to resolve the turbulence close to the wall. The mesh is thus generated to give  $y^+$  values in the range from 30 to 300. The  $k - \varepsilon$  model is a stable turbulence model which often is referred to as the industry standard model. The downsides can be that it is bad at predicting normal stresses which means that it can't take effects of streamline curvature into account or predict stagnation flows.

## 2.2 Computational Fluid Dynamics

Computational Fluid Dynamics (CFD), is nowadays an important tool for simulating flows of all kinds. In the finite volume method the computational domain is divided into a large number of control volumes. The general transport equation

$$\frac{\partial \rho \phi}{\partial t} + \nabla \cdot (\rho \mathbf{u} \phi) = \nabla \cdot (\Gamma \nabla \phi) + \mathbf{S}_\phi \quad (2.13)$$

with  $\phi$  being the quantity needed,  $\rho$  the density,  $\mathbf{u}$  the velocities,  $\Gamma$  is a diffusivity constant and  $\mathbf{S}_\phi$  is a source term. Integrated over each control volume (CV) and time interval  $\Delta t$ , it can be rewritten using Gauss's divergence theorem to a surface integral:

$$\int_t^{t+\Delta t} \left[ \int_{CV} \frac{\partial \rho \phi}{\partial t} dV + \int_A \rho \mathbf{u} \cdot \mathbf{n} dA \right] dt = \int_t^{t+\Delta t} \left[ \int_A \Gamma \nabla \phi \cdot \mathbf{n} dA + \int_{CV} S_\phi dV \right] dt \quad (2.14)$$

where  $\mathbf{n}$  is an outward pointing unit normal of the boundary of the control volume. The first term on the left hand side represents the rate of change of the fluid property  $\phi$  in the control volume and the second term represents the net rate transport of property  $\phi$  out of the volume due to convection. The first term on the right hand side is the net rate transport of property  $\phi$  into the control volume due to diffusion and the last term on the right hand side is the net rate of increase of  $\phi$  due to sources inside the control volume.

In order to then solve the equations, a discretisation of the different terms is needed. This discretisation can be done in different ways, dependent on the physics of the term being discretized. The convection term could for example be discretized with a range of different schemes such as the second order central differencing scheme, first and second order upwind scheme etc.. These schemes are just ways to interpolate the information that is being transported between the cells and the order of each discretization scheme is just a measure of its efficiency and accuracy.

As there is no explicit pressure equation included in the calculations, some type of procedure is needed to couple the pressure with the velocity equations. The SIMPLE and PISO algorithms are methods of dealing with this. These procedures are well covered in literature [18].

## 3 Method

The case setup is based on the swirl generator developed and created at the Polytechnica University of Timisoara in Romania. A mesh was created with the dimensions of the test rig, and then both steady and unsteady simulations were conducted using the OpenFOAM CFD toolbox. The results were later viewed in the visual tool kit *Paraview* and postprocessed using *Matlab* and the two free softwares *Gnuplot* and *Octave*.

### 3.1 Description of the OpenFOAM CFD toolbox

OpenFOAM is an open source CFD software that has the advantage of being open for changes and development. The users can contribute with new ideas and help with extending the software features. OpenFOAM consists of a C++ library, which foremost is used to create *applications*. These applications consist of *solvers* and *utilities*. The solvers are used for solving continuum mechanics problems, and the utilities are mostly used to manipulate data in different forms. The main advantage with OpenFOAM however, is the ease with which you can create and customize solvers. The solver applications are written with OpenFOAM classes, which simplifies the syntax to resemble the partial differential equations that is being used. To be able to make this happen, the programming language needs to have properties such as inheritance, template classes, virtual functions and operator overloading. This is not found in many languages except for a few such as C++ and Fortran-90 [1].

The solvers and utilities are controlled through the use of *dictionaries*. These are files where specifications of the applications are accessed and controlled. Specifications such as discretisation methods, Courant number, start and end time, divergence scheme, turbulence method, pressure corrector settings, linear solver settings and many more are all controlled and accessed through these sets of dictionaries. Running the solvers in parallel, on several processors simultaneously, is done by decomposing the case into as many parts as processors intended for the job. This is easily done in OpenFOAM with the *decomposePar* utility. This utility is also controlled by a dictionary where you can specify in which way to decompose your computational mesh.

When the solver is finally running it will initiate the computations with the values given in a folder named *0*, as in time 0. Then it will print the quantity fields in time folders, with a time interval specified in the dictionary *controlDict*. Residuals are printed in the prompt during computations unless they are specified to be logged in a log file. When the simulations are finished, the case can be reconstructed with the utility *reconstructPar* and postprocessed through the VTK visualization application *paraFoam*.

## 3.2 Numerical Setup

The mesh of the swirl generator, seen in Figure 3.1, is made in ANSYS ICEM CFD with the dimensions given from the test rig. The mesh is made by constructing the four sections: strout blade section, stay vanes section, free runner section and the draft tube section. The parts are then merged together in OpenFOAM with the utility *mergeMeshes*.

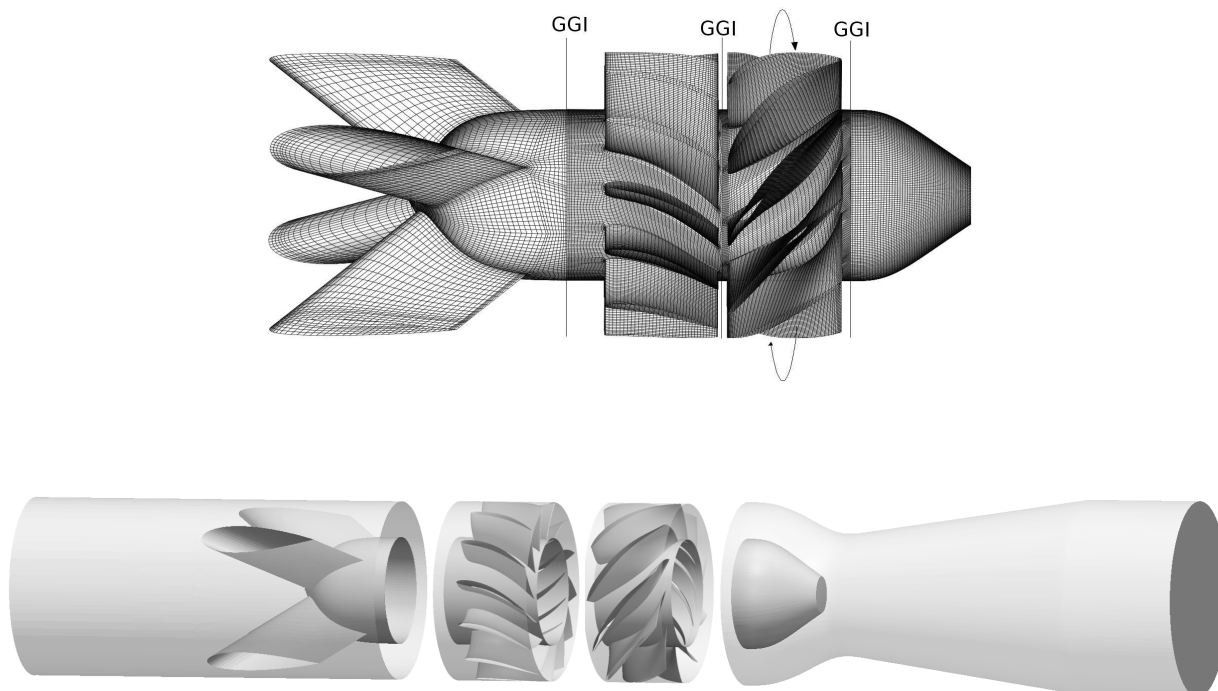


Figure 3.1: Outline of computational domain(bottom) and the merged strout-nozzle, guide vanes, runner and swirl cone (top).

The mesh consists of 2.3 million hexahedral cells where the different parts are coupled through General Grid Interfaces (GGI) [3]. The runner is rotating in the direction shown in the top figure of Figure 3.1 which also show the interfaces which handles the interaction between the rotating part (runner) and the stationary parts (draft tube and guide vanes). At the outlet, the boundary conditions for velocity and turbulence equations are set as a homogeneous Neumann boundary condition. The pressure equation uses a zero mean pressure at the outlet and homogenous Neumann at all other boundaries. For discretizing the convection terms, a second-order upwind scheme is used. In the unsteady simulations, the time derivative terms are discretized using a second-order backward scheme.

### 3.2.1 Steady-State simulations

The inlet flow profile is set as uniform with a volume flow at 30 l/s. To estimate other parameters such as kinetic energy and dissipation, it is usually necessary to estimate the turbulence intensity at the inlet. High turbulence cases usually have a turbulence intensity of 5 % to 10 %. In this case the turbulence intensity is set to 10 % at the inlet. This estimation along with a turbulent viscosity ratio  $\nu_t/\nu$  set to 14.504 is taken from the ERCOFTAC conical diffuser-study [12]. With a general flow discharge of 30 l/s and an inlet area with radius 0.075 m, the inlet boundary conditions becomes:

Table 3.1: Inlet boundary conditions for steady state simulations on the swirl generator.

Variable	Expression	Value	Dimension	Description
$U_z$	$\dot{V}/\pi r^2$	1.6985	$\frac{m}{s}$	Axial Velocity
$k$	$\frac{3}{2}(U_z \cdot I)^2$	0.043274	$\frac{m^2}{s^2}$	Kinetic energy
$\varepsilon$	$(C_\mu k^2)/(\nu \cdot \nu_t/\nu)$	11.623	$\frac{m^2}{s^3}$	Dissipation
$\nu_t/\nu$	$(k^2 C_\mu)/(\varepsilon \nu)$	14.504	[-]	Viscosity ratio
$I$	-	10 %	[-]	Turbulence intensity

A SIMPLE pressure correcting solver with 3 nonorthogonal pressure correctors and relaxation factors set to 0.1 was used in this case. The solver uses a “frozen rotor” approach, which means that for a mesh with rotating parts, the rotating and stationary parts are fixed in relation to each other and the rotation is realized through the use of different frames of reference for the rotating and stationary parts respectively.

### 3.2.2 Unsteady Simulations

The unsteady simulations is the preferred approach in resolving the vortex phenomenon. In order to run unsteady simulations, good initial conditions is needed which can be retrieved by using the results from the steady-state simulations. The URANS equations are then solved and the solver uses a sliding grid approach for the rotor stator interaction, which means that the rotational part of the mesh is actually moving, and the interaction between the moving parts and the stationary parts is made possible with the help of sliding GGI interfaces. The solver uses the PISO pressure correction method, which gives accurate transient solutions but which also is sensitive to the timestep length. Therefore another solver was tested which uses the SIMPLE pressure correction method, and which is far less sensitive to the time step.

## 4 Results and Discussion

The results from the steady-state and unsteady simulations are presented and discussed in the following sections.

### 4.1 Steady-State Simulations

The simulations at steady-state were made at both 870 rpm and 920 rpm. The first rotational speed is because that was obtained when the measurements were conducted. The other rotational speed is because this corresponded to zero torque on the runner, according to Fluent simulations made by Muntean et.al [11]. Both of the cases were initiated using the first-order Upwind scheme until computations were stable, and then continued with the second-order linear Upwind scheme to improve accuracy. The theoretical design profiles used for comparison is based on a theoretic model which should give similar flow conditions to those of a Francis turbine operating at part load. All of the velocity profiles have been circumferentially averaged in order to remove effects of the unsteadiness in the solution.

### 4.1.1 Comparison with theoretical design profiles

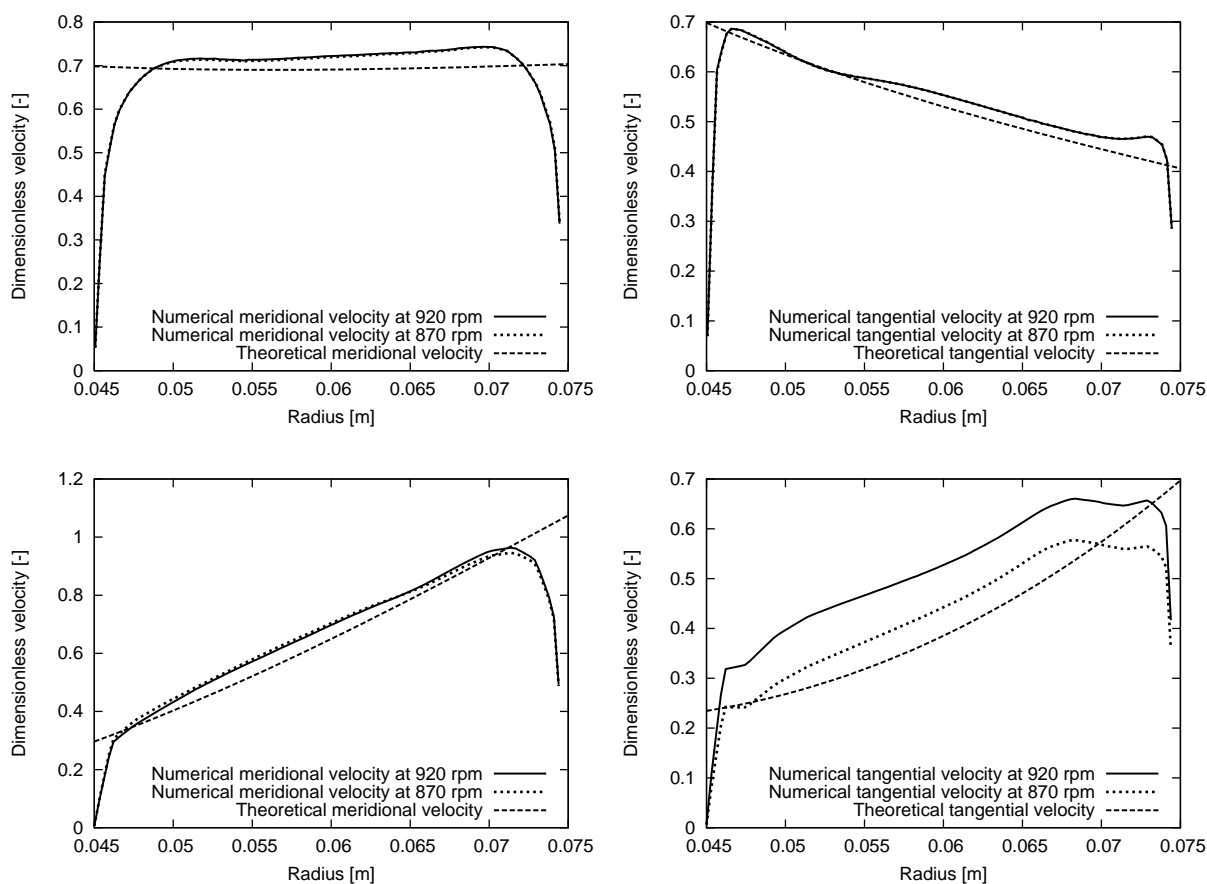


Figure 4.1: Meridional (left) and tangential (right) velocities at cross-sections 1 (top) and 2 (bottom), compared with the theoretical design profile for each section.

Figure 4.1 show the velocity profiles at cross-sections 1 and 2, with section 1 located between the guide vanes and the runner and section 2 located downstream the runner. The results are compared with the theoretical design profiles from the blade design study by Resiga et.al [15]. The numerical results show a good agreement with the design profiles. In the case with a rotational speed of 870 rpm, the tangential velocity at cross-section 2 is in good agreement with the theoretical design profile. However, it is not reaching its intended value near the shroud, and in the case of 920 rpm, the tangential velocity is overestimated compared to the theoretical profile design. This means that a rotational speed of 920 rpm is too high and that 870 rpm will more accurately create a swirling flow that corresponds to the flow estimated by the theoretical model. As seen in Figure 4.1, the two numerical velocity profiles show a very similar shape to each other. This similarity indicates that the deviation at the shroud is not dependent of the rotational speed, and that it's more likely caused by the computational model.

### 4.1.2 Comparison with LDV measurements

Comparison with LDV measurements for both rotational speeds is shown in Figure 4.2. The data is presented in dimensionless values where the used references are the minimum radius of the throat and the mean velocity at the throat. (see Figure 1.3 to see where the location of the survey axes are)

$$R_{throat} = 0.05 [m], \quad v_{throat} = \frac{\dot{V}}{\pi \cdot R_{throat}^2} [m/s]$$

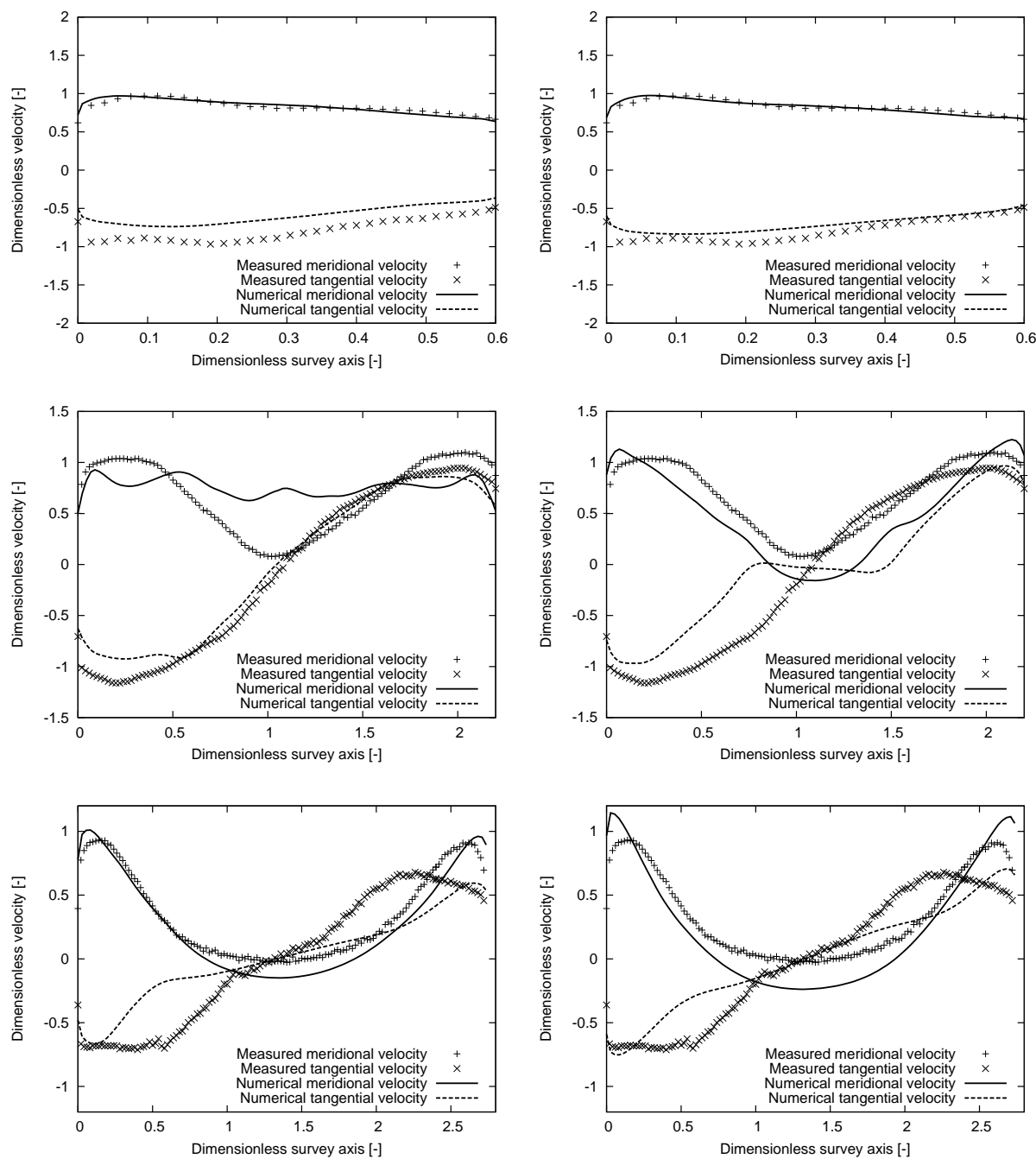


Figure 4.2: Comparison with meridional and tangential velocities between simulations at 870 rpm (left) and 920 rpm (right). Velocities are compared at survey axis 0 (top plots), survey axis 1 (middle plots), and survey axis 2 (bottom plots).

At survey axis 0 in the top left plot of Figure 4.2, a good agreement with the measurements is shown for the meridional velocity. The tangential velocity is however underestimated, which indicates that the rotational speed of 870 rpm is erroneous. The shape of the predicted velocity profile is very similar to that of the measurements which means that the solution method still works well for that part of the swirl generator and that the lack of fit are due to the incorrect rotational speed. This conclusion is strengthened by the top right plot of Figure 4.2, where the resulting tangential velocity from a rotational speed of 920 rpm on the runner show much better agreement with the measurements.

At survey axis 1, the meridional velocity profile (middle left plot of Figure 4.2) for the rotational speed 870 rpm, is shown to deviate alot from the measurements. Why it looks like this is hard to tell, since there's not even a stagnation region for the meridional velocity which can be seen in the measurements. However, it is clear that the rotational speed has a big impact on the swirl profile. The tangential velocity is in good agreement with the measurements. There are some deviations close to the walls of the draft tube, which probably comes from the error in rotational speed and perhaps also the same source of error discussed for the design profile plot in Figure 4.1. The correctness of these results can however be discussed, since the prediction of the meridional velocity makes little sense, which means that the tangential velocity could be erroneously predicted as well. For a rotational speed of 920 rpm at survey axis 1 (middle, right plot of Figure 4.2), there is a quite large deviation for the numerical tangential velocity profile, and for the measurements there is a stagnation region in the center of the draft tube. This stagnation region is predicted to be a recirculating region in the simulations. One probable cause of this could a misprediction of the turbulence in that part of the draft tube. Since the  $k - \varepsilon$  turbulence model has trouble predicting streamline curvature effects in the flow, it is possible that this causes the stagnation region to be overpredicted and instead become a recirculating region.

Further downstream the draft tube, at survey axis 2, the deviation of the numerical tangential velocity is again very large and it seems that a lot of swirl have been lost this far down the draft tube. The error in tangential velocity is reduced some when the rotational speed is increased from 870 rpm to 920 rpm, but this causes the meridional velocity to deviate even more.

The results so far, have shown that the flow seem to have unsteady flow properties which cannot be resolved by the steady-state simulations. At survey axis 0 for example, the effects of the vortex rope are small, which also reduce the importance of the transient term. Therefore the results fit quite well with the LDV measurements. At the survey axes 1 and 2, there are significant differences and it seems that the steady-state solver cannot handle what is happening downstream the throat. The most lack of fit occurs at survey axis 1, where the unsteady vortex rope has most influence on the flow.

### 4.1.3 Comparing moment forces

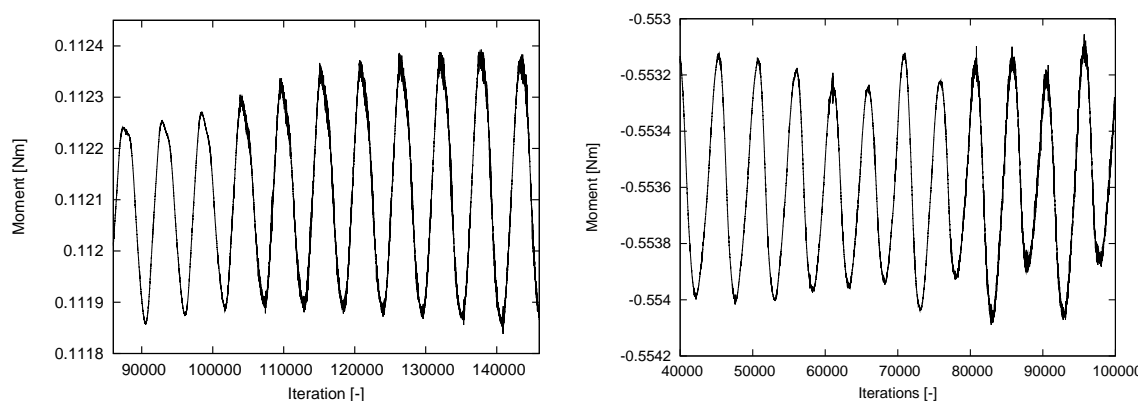


Figure 4.3: Moment acting on the runner at 870 rpm (left) and 920 rpm (right).

Figure 4.3 shows the axial moment acting on the runner during the simulations at 870 rpm and 920 rpm. For a rotational speed of 870 rpm, the mean moment acting on the runner is about -0.5536 Nm (with the z-axis as the reference direction) whereas the results for a rotational speed of 920 rpm gives a mean moment of about 0.1121 Nm. Since the z-axis is directed downwards, a negative moment indicates that the runner is spinning too fast and that it is consuming (at the tip) more energy than it is extracting (at the hub) from the flow. The moment is therefore directed in the negative z-direction to make the runner rotate slower. A positive moment is implying the opposite, which means that the moment is directed in the positive z-direction to make the runner rotate faster. Seen from another perspective, this also means that in order to maintain the rotational speed, it is either needed to add power (if the moment is positive), or in some way apply a breaking force to stop the runner from accelerating (if the moment is negative). In order to make a good comparison with measurements later, it is desired to not need any interference, which is the case when the runner is rotating completely free.

The fluctuations in Figure 4.3 is caused by a small vortex rope in the draft tube. As can be seen in the figure, the simulations for the rotational speeds 870 rpm and 920 rpm takes about 120000 and 80000 iterations respectively, which is quite a lot when running steady-state cases. The cause of this could be that since there is a developing disturbance in the system, the flow conditions are constantly changing and thus causing the global premise for solution to change as well. The flow is inherently unsteady, and it makes it impossible for the solution to converge into a steady-state solution.

Summarizing this, it is seen that for 870 rpm, both the moment acting on the runner and the comparison with measurements indicates that the rotational speed is erroneous. For 920 rpm, the comparing with the measurements implies almost correct rotational speed and the moment acting on the runner implies an incorrect rotational speed. These results are in conflict with each other, and together with the misprediction shown for both cases, it can be concluded that this method for solution is unaccurate and insufficient when resolving the flow in the swirl generator.



## 4.2 Unsteady Simulations

The solver for the unsteady simulations uses the feature of a sliding grid to simulate the rotor stator interaction and the PISO algorithm for coupling the pressure with the velocity equations. The simulations are made at a rotational speed of 870 rpm, 920 rpm and 890 rpm, where 890 rpm is obtained from linear interpolation of the results of 870 rpm and 920 rpm. A solver which uses the SIMPLE algorithm is tested and compared to the PISO based solver. The initial conditions for all cases, are taken from the results of the steady state simulations. For the case at 890 rpm, the steady-state results from the 870 rpm simulations was used.

The simulations at 870 rpm were realized using a time step of  $1.3 \times 10^{-4}$  s, yielding a maximum Courant number of 2.79. For the simulations with 920 rpm and 890 rpm, the timestep was  $1.4 \times 10^{-4}$  s and  $1.2 \times 10^{-4}$  s respectively, giving a maximum Courant number of 3 at 920 rpm and 2.5 at 890 rpm. The numerical velocity profiles are all averaged circumferentially and in time.

### 4.2.1 Comparison with theoretical design profiles

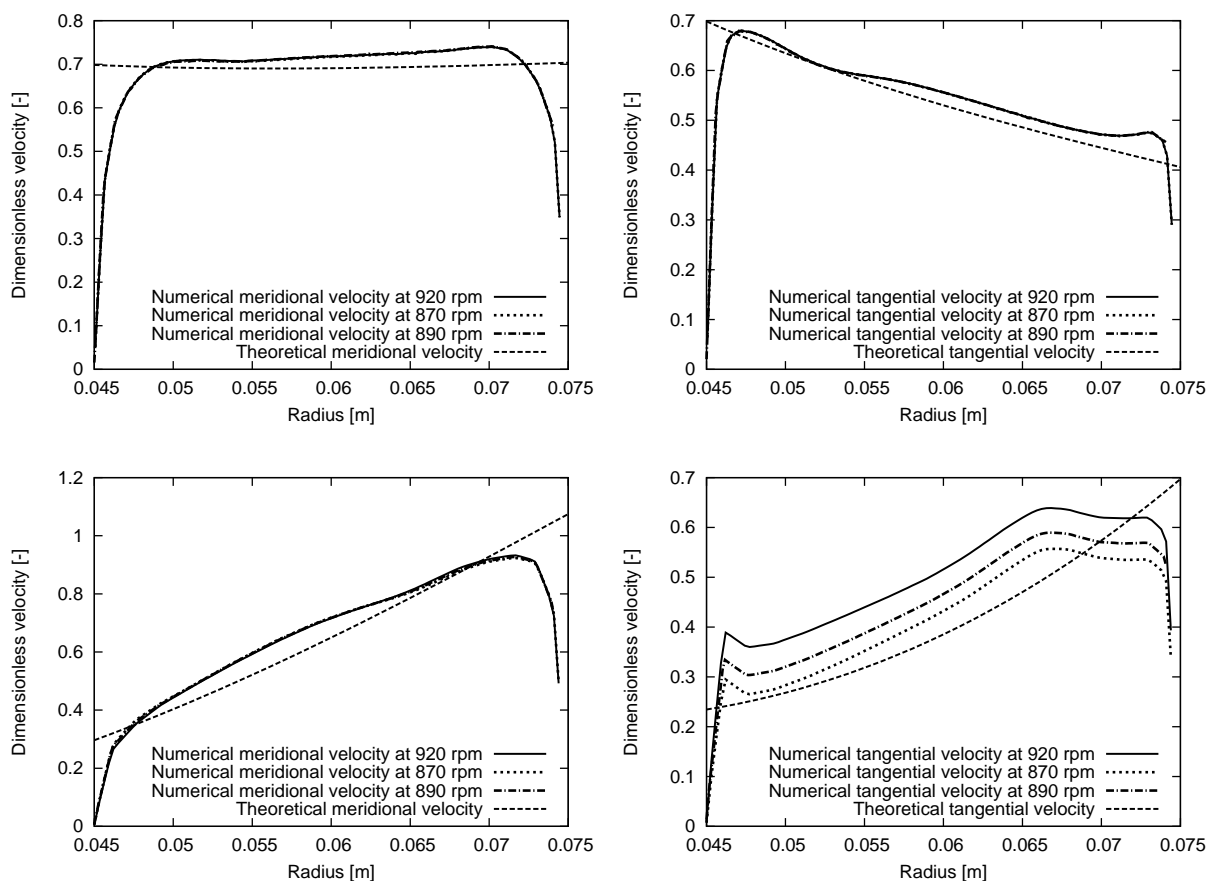


Figure 4.4: Meridional (left) and tangential (right) velocities at cross-sections 1 (top) and 2 (bottom), compared with the theoretical design profile for each section.

Figure 4.4 show the comparison at cross sections 1 and 2 (see Figure 1.2). The averaged velocity profiles for all rotational speeds are compared with the theoretical design profile for the swirl generator. The plots in Figure 4.4 show very similar results to those of

the steady-state simulations. The numerical velocity profiles are in good agreement with the theoretical design profiles and the tangential velocities at cross-section 2 are again deviating close to the shroud. The fact that the velocity profiles show these similarities with the steady-state results means that unsteady effects in this part of the flow is very small, and so the unsteady term in the equations gives little change to the solution. As for the steady-state results, simulation with the rotational speed of 870 rpm gives the best agreement. When the rotational speed is increased, so is also the error in tangential speed.

#### 4.2.2 Comparison with LDV measurements

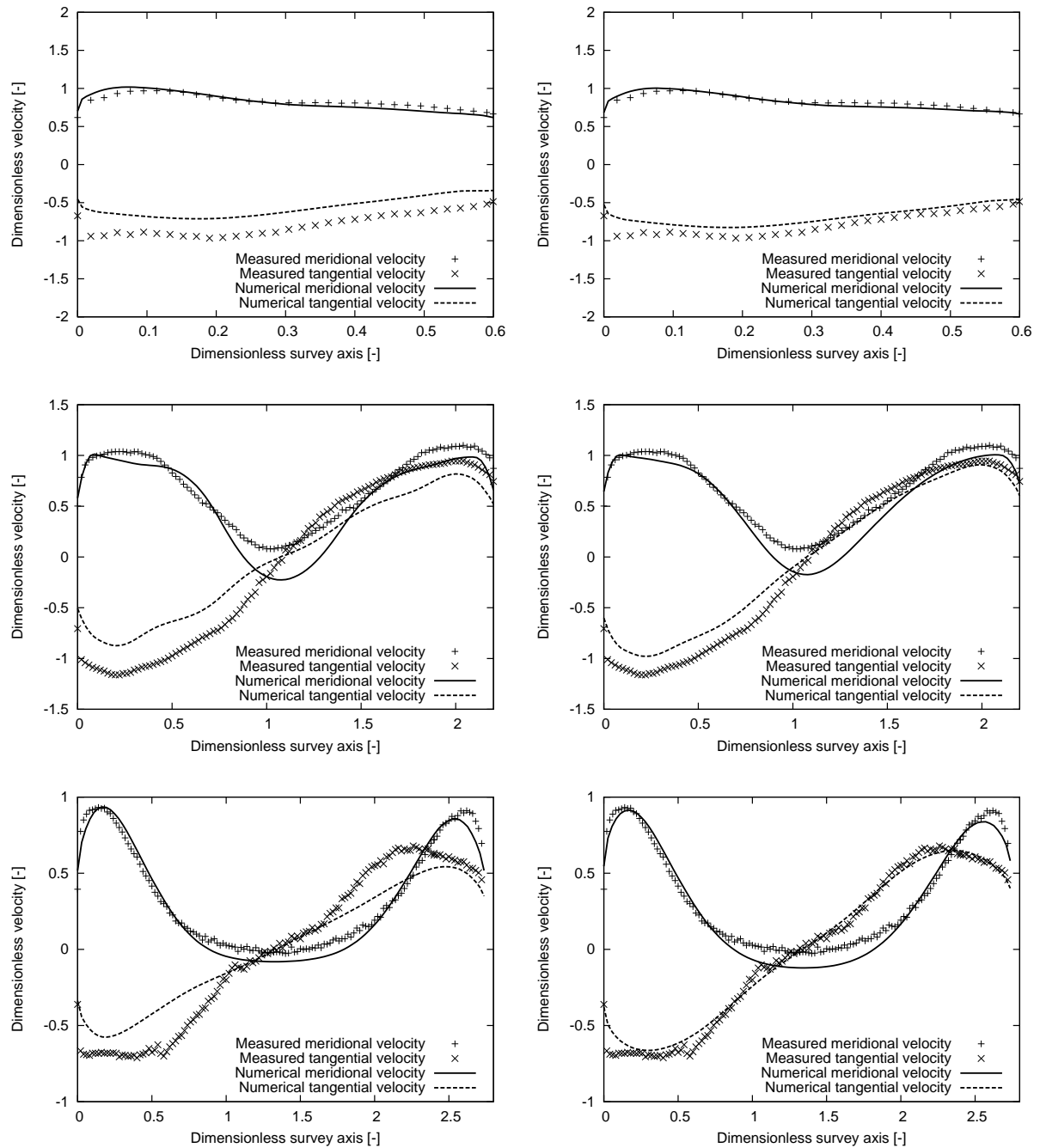


Figure 4.5: Comparison for meridional and tangential velocities between simulations at 870 rpm (left) and 920 rpm (right).

Figure 4.5 shows the comparison with LDV measurements for the cases of 870 rpm and 920 rpm. It is shown that both tangential and meridional velocity show much better agreement with the measurement values than the steady state simulations. The velocity profiles at survey axis 0 (top of Figure 4.5) is as in the steady-state case, in good agreement with the measurements. The shape of the tangential velocity profile is somewhat more accurately resolved, and the main error is the magnitude of the velocity which is caused by an error in rotational speed. At survey axis 1, the results show a deviating tangential velocity at the wall, and a recirculating region for the meridional velocity in the center of the draft tube. When the rotational speed is increased from 870 rpm to 920 rpm, this recirculating region is reduced to some extent, however not enough to conclude this to be the only source of error. Instead, it is more likely that the computational model is the main cause of this deviation. The tangential velocity at survey axis 1 reveals the same deviation close to the wall for both rotational speeds. The error is reduced when increasing the rotational speed to 920 rpm, as shown when comparing the middle plots of Figure 4.5. The tangential velocity at survey axis 2 (bottom plots) is shown to be greatly influenced by the rotational speed on the runner, and the error is reduced substantially for the same change in rotational speed.

### 4.2.3 Comparison between the PISO based solver and a SIMPLE based solver

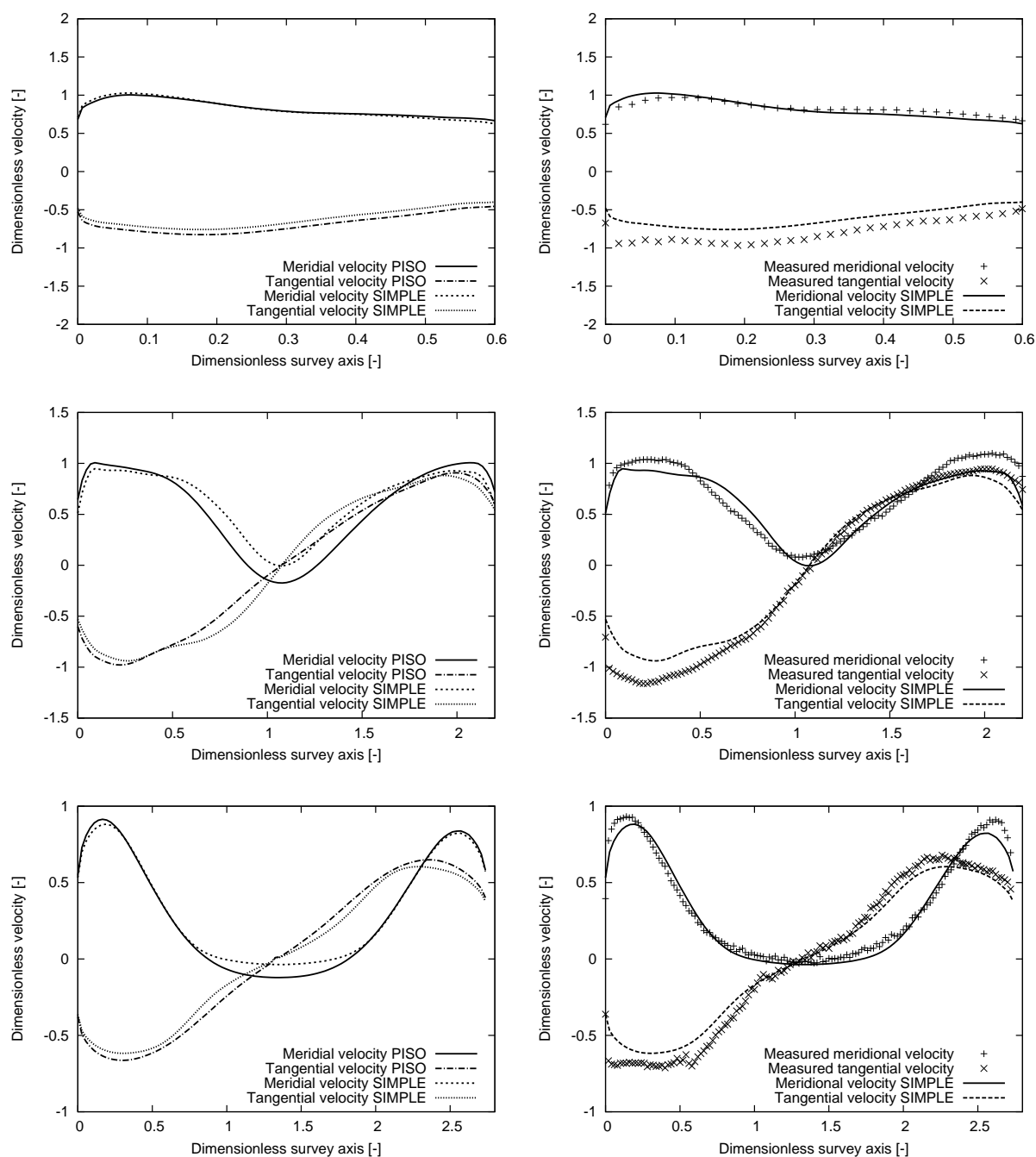


Figure 4.6: Comparings with tangential and meridional velocities between SIMPLE and PISO based solver (left), and comparings of SIMPLE with measurements(right). Velocities are compared at survey axis 0 (top), 1 (middle) and 2 (bottom).

Figure 4.6 shows the results of simulations made with the SIMPLE based solver. It is shown in comparison to the PISO based solver used in the previous simulations and the comparison reveals a distinct difference between the solvers. Noticeable here is that the SIMPLE based solver don't give any recirculating area where the PISO based solver do. Also the tangential velocity profile in the top of Figure 4.6 seems more similar to that of measurements than the PISO based solver. For the results of the PISO based solver,

the tangential velocity in the center part of the draft tube looks more like a straight line, and it seems that the solver don't predict this "s"-shape, shown in the measurements. The SIMPLE based solver seems to be resolving this. The comparison with measurements downstream the throat, at survey axis 1 and 2, show a very good agreement. There is still a deviation close to the wall, but this has been concluded to be caused by an error in rotational speed rather than the computational model, which makes these results the best so far. The SIMPLE method for coupling the pressure with the velocity equations are usually considered the more stable method out of the two. This stability is often achieved at the expense of accuracy, and so the results from using this method should be less accurate than using PISO. The results are interesting, but further investigation is needed in order to conclude that the SIMPLE based solver really gives a better prediction and that these results are not caused by "inaccuracy" instead of accuracy.

#### 4.2.4 Comparison of moment forces and pressure fluctuations

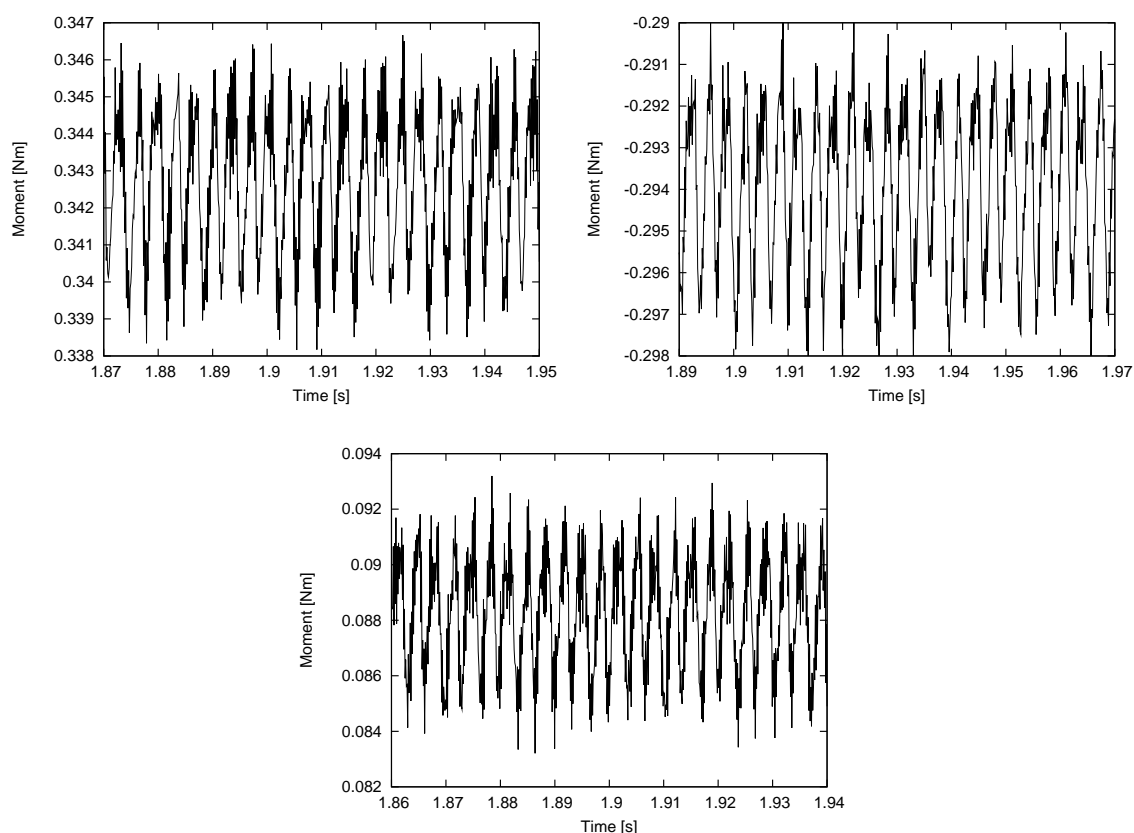


Figure 4.7: Moment acting on the runner at 870 rpm (top left), 920 rpm (top right) and 890 rpm (bottom).

Figure 4.7 show the moment acting on the runner for the three cases 870 rpm, 920 rpm and 890 rpm at stabilized unsteady simulations. The results from 870 rpm show a positive mean moment of about 0.343, and the results from 920 rpm show a negative mean moment of -0.294, which indicates that the rotational speed corresponding to a torque equal to zero lies between 920 rpm and 870 rpm. Linear interpolation of the results from these two rotational speeds with respect to the forces acting on the runner, gives a rotational speed of 890 rpm which should correspond to zero axial moment. The velocity profiles of the simulations at 890 rpm don't show anything of interest. The only interesting results from that

simulation is the moment acting on the runner, shown in the bottom plot in Figure 4.7. It is seen that for 890 rpm, the mean moment acting on the runner is approximately 0.088 Nm. This is not sufficient to conclude that 890 rpm is the correct rotational speed, but it is however a close value and it should give very similar flow conditions as the rotational speed that do give a torque equal to zero. The rotational speed could be better estimated doing one additional linear interpolation, or maybe use another method to pinpoint where the moment will be zero.

Several frequencies can be observed in the plots of Figure 4.7. At least 3 frequencies can be seen: One low frequency, one intermediate frequency and one high frequency which all are caused by the pressure fluctuations in the system. Therefore, the pressure is analysed in the following section to see where these frequencies originates from.

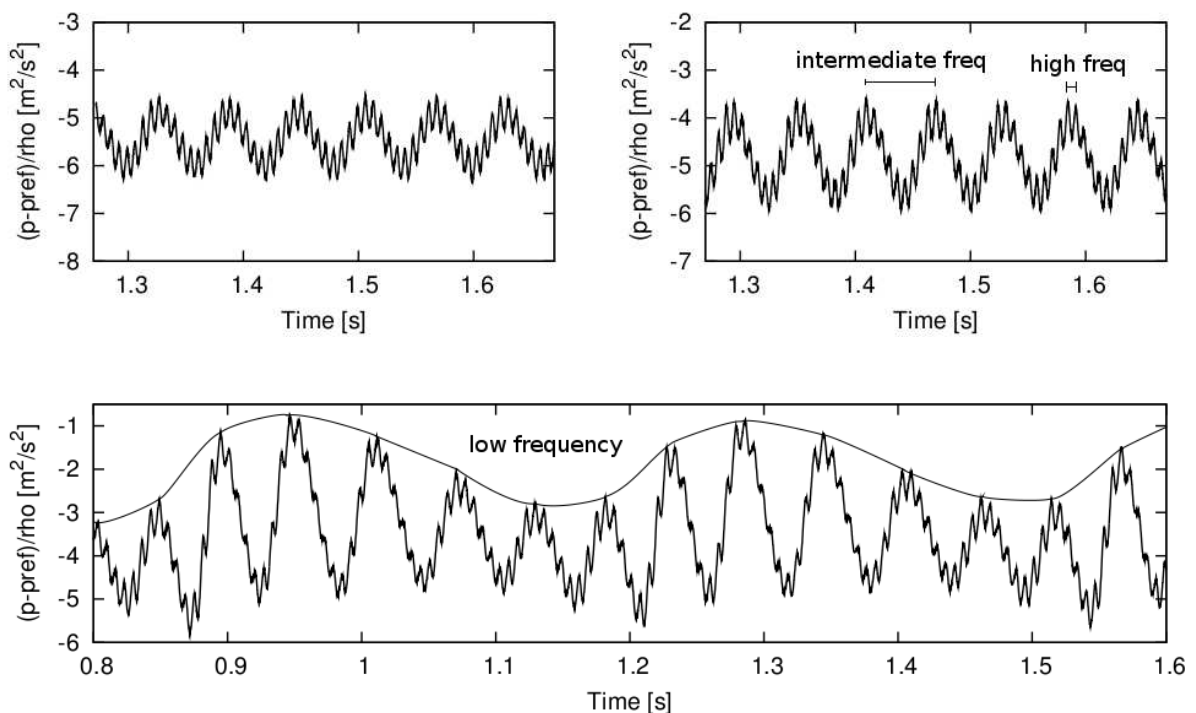


Figure 4.8: Pressure at MG0 for rotational speeds of 870 rpm (top left), 890 rpm (top right) and 920 rpm (bottom).

Figure 4.8 show the pressure oscillations at the throat (MG0, see Figure 1.3) for the the rotational speeds 870 rpm, 890 rpm and 920 rpm. The intermediate frequency, that can be clearly seen in all three plots, is caused by the vortex rope in the draft tube which is rotating at almost the same rotational velocity as the runner. A rotational speed of 920 rpm is the same as 15.33 turns/second which should correspond to a pressure frequency of 15.33 Hz. The higher frequency is caused by the rotor stator interaction. With 13 guide vanes and 10 runner blades rotating at a velocity of 15.33 turns/second (920 rpm), the number of runner blades that passes one guide vane per second is  $15.33 \cdot 10 = 153.3$  blades/second, which should correspond to a frequency of 153.3 Hz in the pressure fluctuations. The lower frequency, here only seen in the plot for 920 rpm, is caused by axial movement of the vortex rope. In the bottom plot of Figure 4.8 it can be seen that one period of this low frequency,

corresponds to 5 periods of the intermediate frequency, which is the same as 5 turns of the runner, with each turn having a period of  $1/15.33 = 0.0652$  s, the period for the lower frequency would be  $5 \cdot 0.0652 = 0.326$  s. These periods are just the time intervals that the pressure fluctuations should have, if it was following the motion of the runner directly, and the simulation show that they almost do. The definite frequencies of the predicted pressure fluctuations are estimated in the fourier analysis in section 4.3.

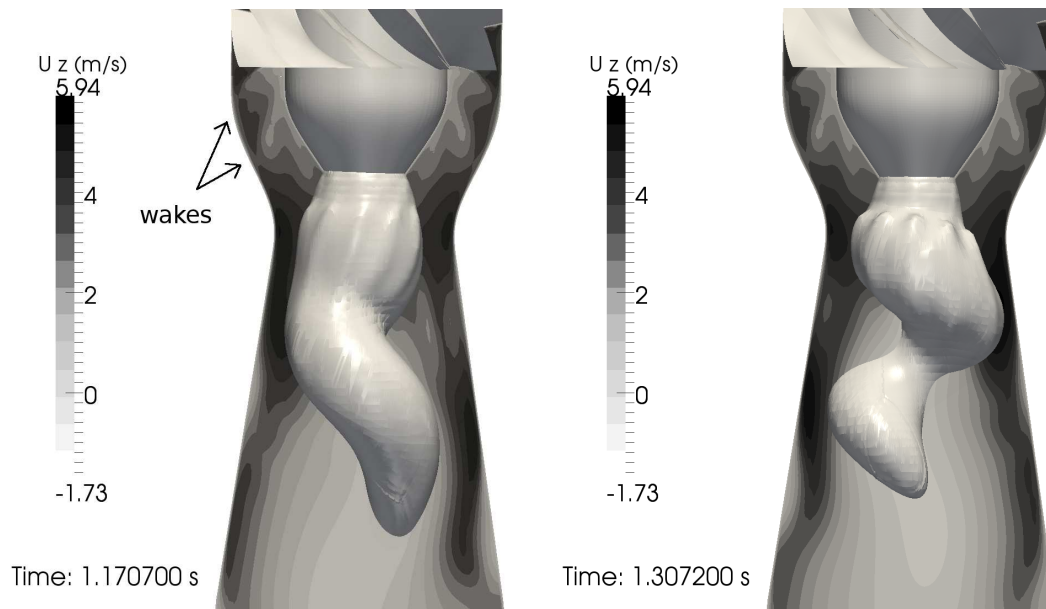


Figure 4.9: Vortex rope at a rotational speed of 920 rpm at 1.17 s(left), and 1.3 s(right).

Figure 4.9 show the vortex rope of the 920 rpm- simulations at two different time steps. It shows the retraction and extraction of the vortex rope that is causing the low frequency seen in the pressure fluctuations. Comparing with the bottom plot in Figure 4.8, it can be seen that the amplitude has reached its min value when the vortex rope has extended itself to a maximum (1.17 s). When retracted to max (1.3 s), the fluctuations reaches its maximum value. This movement have not been seen in the measurements, so even if there is a good agreement at 920 rpm for the velocity profiles in the draft tube, the simulations seems to be predicting a different movement of the vortex rope compared to what is seen in the measurements. It is hard to tell why this is, but as this low frequency is not seen for the simulations at 870 rpm or 890 rpm, it seems that something is happening between 890 rpm and 920 rpm that highly influences the movement of the vortex rope. Another thing to notice in Figure 4.9 is that the simulations are resolving the wakes coming from the runner into the convergent part of the draft tube. These wakes are resolved on the isosurface as well, seen as small ripples in the throat region of the draft tube. In the center of the draft tube, the recirculation region can be seen. This region is extended almost all the way up to the throat.

### 4.3 Fourier Analysis

An analysis of the pressure fluctuations at MG0, MG1, MG2 and MG3 will be covered in the following section. Muntean et al. [11] made a fourier analysis on Fluent and OpenFOAM simulations and compared them with measurements. The present analysis is made in Matlab using the built-in Fast Fourier Transform algorithm and the pressure values are taken at the transducer locations (see Figure 1.3) for the best fitted results, which was the unsteady 920 rpm simulation.(with the PISO-based solver)

#### 4.3.1 Fourier analysis theory

Given periodic function  $f(t)$  with period  $T = 2L$  seconds, then the function  $f(t)$  can be decomposed into a sum of components of sine and cosine functions as:

$$g(t) = \frac{a_0}{2} + \sum_{n=1}^{\infty} \left[ a_n \cos\left(\frac{\pi n t}{L}\right) + b_n \sin\left(\frac{\pi n t}{L}\right) \right] \quad (4.1)$$

where

$$a_0 = \frac{1}{2L} \int_{-L}^L f(t) dt, \quad a_n = \frac{1}{L} \int_{-L}^L f(t) \cos\left(\frac{n\pi t}{L}\right) dt,$$

$$b_n = \frac{1}{L} \int_{-L}^L f(t) \sin\left(\frac{n\pi t}{L}\right) dt$$

and  $a_0$  is the mean value of  $f(t)$ .  $a_n$  and  $b_n$  are the sine and cosine mode amplitudes, respectively, for the angular frequency  $\frac{\pi n}{L}$ . This can also be expressed in the complex form:

$$g(t) = \sum_{-\infty}^{\infty} c_n e^{i \frac{\pi n t}{L}} \quad (4.2)$$

$$c_n = \frac{1}{2L} \int_{-L}^L f(t) e^{-i \frac{\pi n t}{L}} dt, \quad n = 0, 1, 2, 3, \dots, N-1 \quad (4.3)$$

A vector with N complex numbers  $\mathbf{x}_n = [x_0, x_1, \dots, x_{N-1}]$  can then be transformed into a frequency domain representation,  $\mathbf{X}_k = [X_0, X_1, \dots, X_{N-1}]$  by the Discrete Fourier Transform (DFT), defined as:

$$X_k = \sum_0^{N-1} x_n e^{-\frac{2\pi i}{N} kn}, \quad k = 0, 1, \dots, N-1 \quad (4.4)$$

and transformed back again using its inverse (IDFT), which is defined as:

$$x_n = \frac{1}{N} \sum_0^{N-1} X_k e^{\frac{2\pi i}{N} kn}, \quad n = 0, 1, \dots, N-1 \quad (4.5)$$

The DFT can be calculated using a Fast Fourier Transform algorithm.



### 4.3.2 Fourier algorithm in Matlab

Matlab uses a FFT algorithm called the Cooley- Tukey Fast Fourier Transform algorithm [7]. From the definition of eq. (4.2) it can be seen that the calculation of  $X_k$  requires  $N$  operations that involves multiplication of two complex numbers followed by the addition of two complex numbers. The transformation of the vector  $\mathbf{x}_n = [x_0, x_1, \dots, x_{N-1}]$ , requires a total of  $N^2$  of these operations. If  $N$  is large, which usually is the case in numerical investigations,  $N^2$  is a lot higher, which makes the calculations hard to manage. Then, if  $N$  is not a prime, it can be decomposed into  $N = N_1 N_2$  and then  $N_1$  transforms of size  $N_2$  can be computed, followed by a computation of  $N_2$  transforms of size  $N_1$  and so on until the problem can be solved [8, 9]. This is what the Cooley- Tukey FFT algorithm does. It computes the fft and inverse fft pair for given vectors of length  $N$  by:

$$fft(x_j) = X_k = \sum_{j=1}^N x_j e^{\frac{-2\pi}{N}(j-1)(k-1)} \quad (4.6)$$

$$ifft(X_k) = x_j = \frac{1}{N} \sum_{k=1}^N X_k e^{\frac{2\pi}{N}(j-1)(k-1)} \quad (4.7)$$

for each number  $x_j$  and each transformed number  $X_k$ .

The fourier transformed values can then be plotted in a power spectrum where the squared absolute value of the coefficients are plotted against the frequencies. The absolute values of the coefficients are the distance of the complex number to the origin, and since each complex number produced by the FFT has a complex conjugate, the power and frequency is calculated using only half of the transformed values.

$$power = |X_k|^2 \quad k = 1, 2, 3, \dots, (N - 1)/2 \quad (4.8)$$

$$f = n_j/\Delta t \quad j = 1, 2, 3, \dots, (N - 1)/2 \quad (4.9)$$

where  $n_j$  is the  $j$ :th sample on the sampling time interval  $\Delta t$ .

To compare the pressure fluctuations dimensionally, the Strohaul number can be calculated:

$$St = \frac{f \cdot l}{V} = \frac{f \cdot D}{\left(\frac{4 \cdot Q}{\pi \cdot D^2}\right)} \quad (4.10)$$

where  $D$  is the the reference length, i.e. the throat diameter = 100mm,  $Q$  is the total discharge of 30 l/s, and  $f$  is the fundamental frequency, in this case the vortex frequency.

### 4.3.3 Results of fourier analysis

Plots of the pressure history at locations MG0, MG1, MG2 and MG3 are shown in Figure 4.10. The plots show the signal plotted against time for two periods of the lowest frequency, which is  $2 \cdot 0.326 \text{ s} = 0.652 \text{ s}$ . The FFT reconstructed signal is also shown for the same time period.

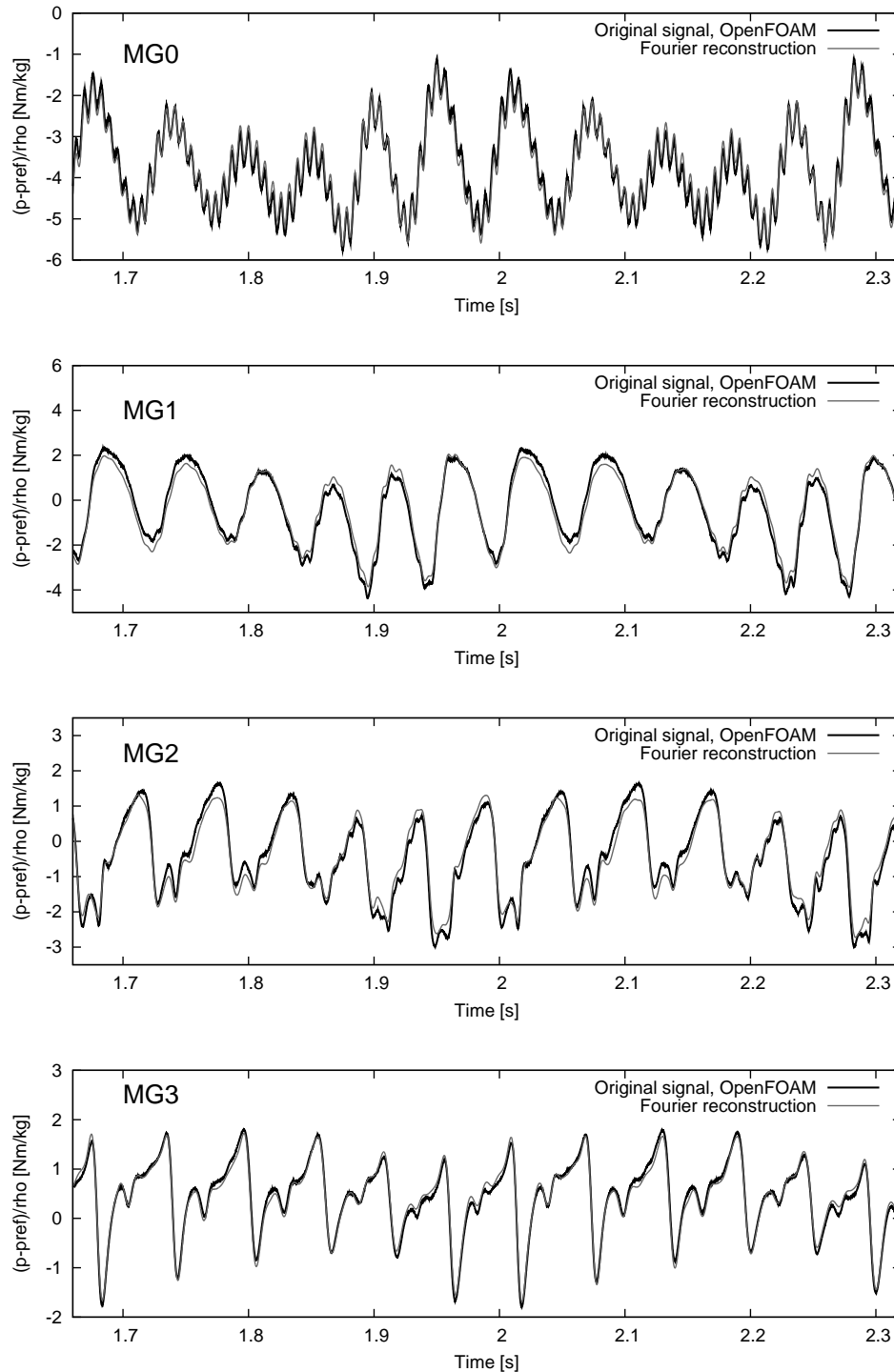


Figure 4.10: Unsteady pressure at pressure transducers MG0, MG1, MG2 and MG3, and fourier reconstructions.

Figure 4.10 shows the fluctuating static pressure at the locations of the transducers seen in Figure 1.3. Both the lower and intermediate frequency can be seen in all of the plots. The higher frequency, which comes from the rotor stator interaction, is mostly resolved at the throat (MG0). At MG1 and MG2, the high frequency can be seen as well, even though its amplitude is not of the same order of magnitude. The pressure fluctuations below the throat is dominated by the low and intermediate frequencies, which is caused by the rotation and axial movement of the vortex rope. Reconstruction of the signals was done using 72 modes for MG0, 100 modes for MG1, 130 modes for MG2 and 90 modes for MG3. The reconstruction was done by applying the Matlab ifft algorithm, and including the fourier coefficients which was shown to have the highest power in order of magnitude. So if a signal is reconstructed using 10 modes, this means that only the 10 coefficients that have the highest absolute values is included in the reconstruction. In this way, the fundamental frequencies of the signal will be included first so that the amount of modes needed for reconstruction can be estimated effectively.

Comparisons are made with a previous OpenFOAM simulation made by Muntean et.al [11] which was made only on the draft tube. The pressure fluctuations for this study is shown in Figure 4.11. Here the same matlab FFT and IFFT algorithm have been used to reconstruct the pressure signal, with 7 modes for MG0, 20 modes for MG1, 44 modes for MG2 and 50 modes for MG3.

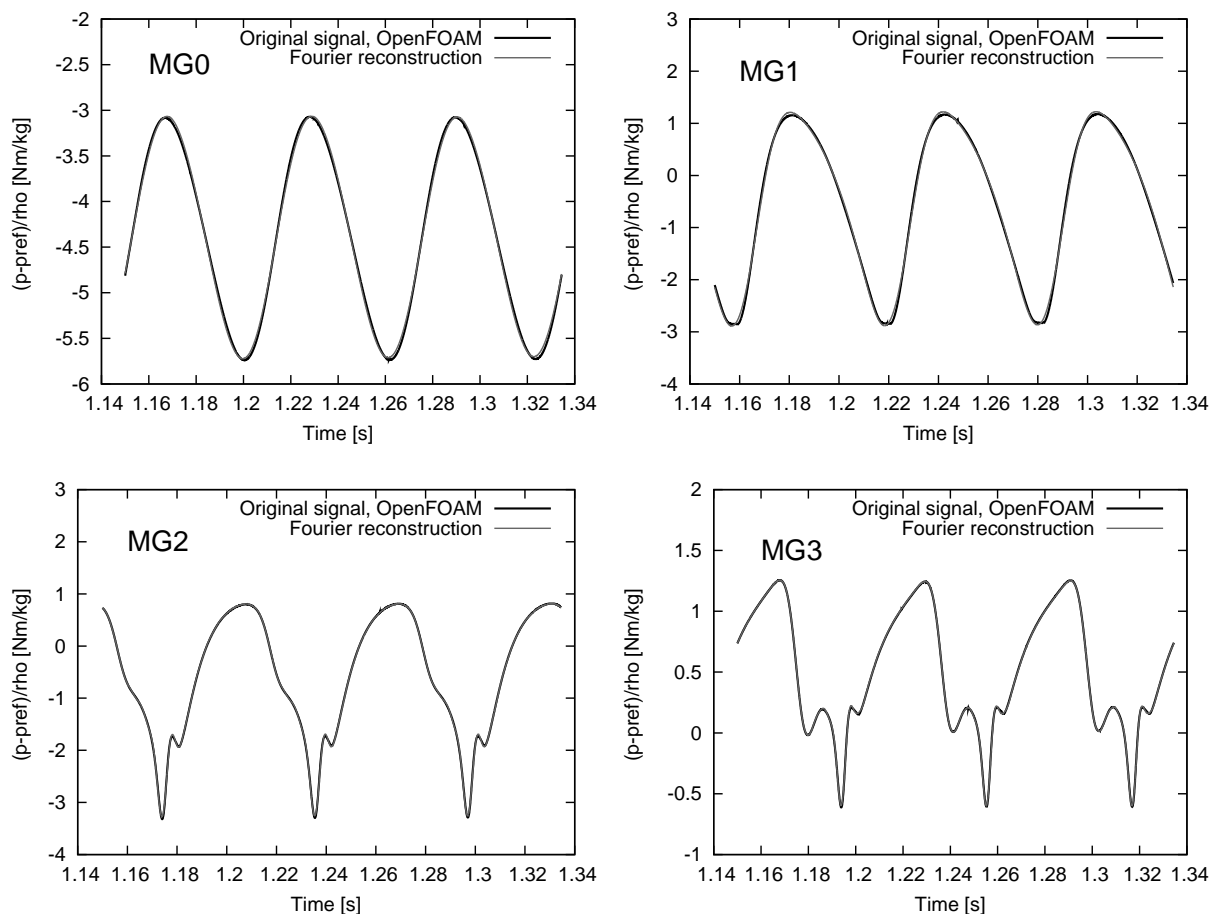


Figure 4.11: Unsteady pressure from the previous study at pressure transducers MG0, MG1, MG2 and MG3, and fourier reconstructions.

The pressure oscillations shown in Figure 4.11 has no lower or higher frequencies included in the pressure fluctuations, which is because this case was run on the draft tube only, without the effects of the runner included in the simulations.

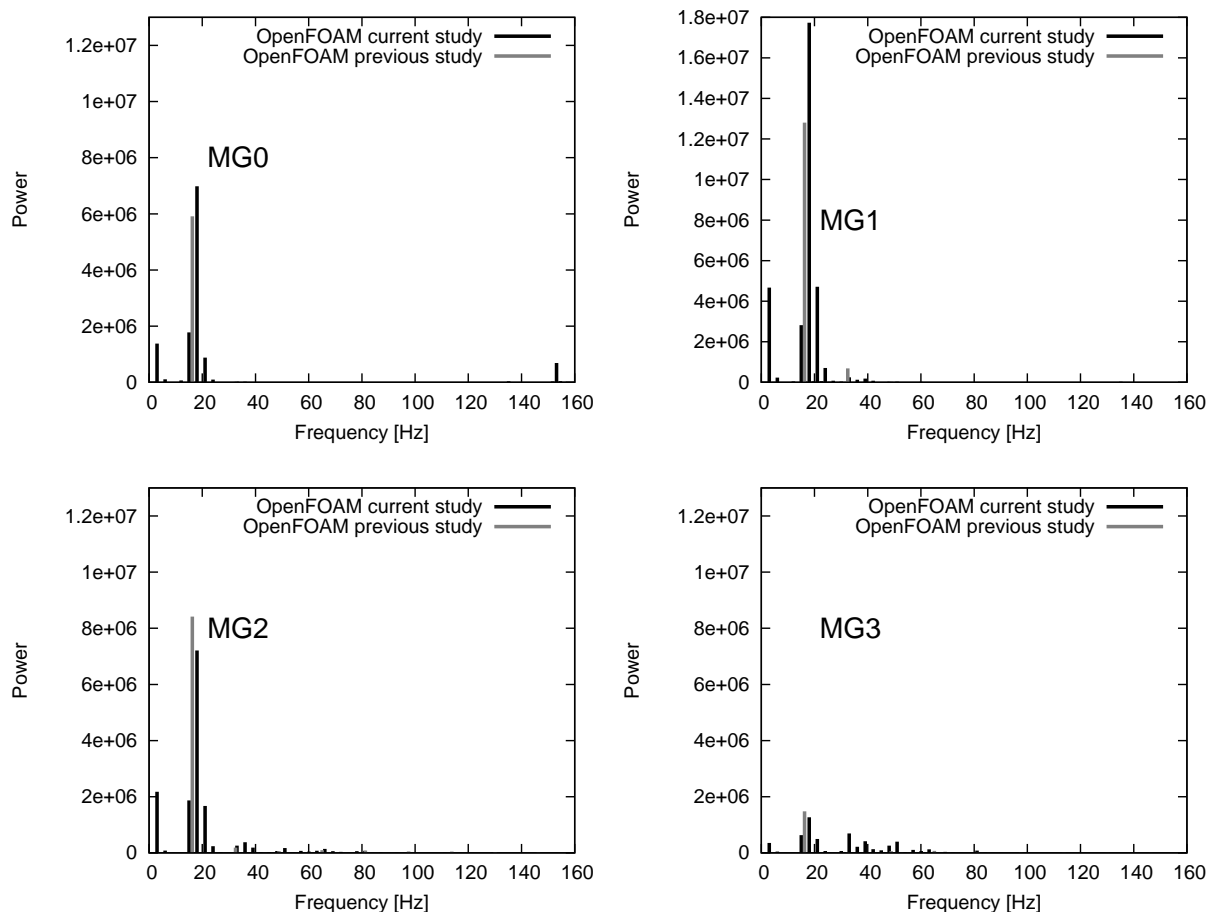


Figure 4.12: Frequency spectra at transducer locations  $MG0$ ,  $MG1$ ,  $MG2$  and  $MG3$ .

The frequency spectra in Figure 4.12 show a comparison with the previous OpenFOAM simulation made by Muntean et.al. [11]. That study showed results that was in good agreement with the measurements, even though the harmonics were slightly overestimated. At  $MG0$ , the amplitude of the 1<sup>st</sup> harmonic is almost in the same order of magnitude as the previous study. It is seen at a frequency of 18.02 Hz, which is the same as the intermediate frequency for 920 rpm shown in the bottom of Figure 4.8. Also, the low and high frequencies discussed previously can be seen as the harmonics at 3.0 Hz and 153.19 Hz respectively. At  $MG1$ , the difference in amplitude for the 1<sup>st</sup> harmonic has increased and the present study show an amplitude about 1/3 part higher than the previous study. The harmonics for the higher frequency harmonic at 153.19 Hz is not seen any more, and the low frequency harmonic has been elevated. At  $MG2$ , the amplitude of the 1<sup>st</sup> harmonic is again in good agreement with the previous study. The low frequency harmonic at 3 Hz is shown here as well with a slightly lower amplitude than at  $MG1$ . Good agreement is also shown at  $MG3$  for the 1<sup>st</sup> harmonic amplitude. The vortex ropes frequency is 18.02 Hz, which corresponds to a Strohau number of 0.480. The Strohau number of the previous study was 0.427.

## 5 Conclusion

Meshing, steady and unsteady state simulations have been conducted on a swirl generator. The meshing have been made with ANSYS ICEM-Hexa, and the computational domain have been acknowledged for running simulations that can be comparable with LDV data. Then steady state simulations at two different rotational speeds have been made, using the standard  $k - \varepsilon$  model to close the equations. The steady state simulations from both rotational speeds are not accurately resolving the flow profiles. They serve as a good initial conditions for unsteady simulations, but can't be used alone to predict the flow features. Unsteady state simulations were conducted at three rotational speeds in order to find the one corresponding to zero torque on the runner, and to compare the results from that rotational speed with LDV measurements. The results showed that unsteady CFD simulations accurately predicts the flow field of the swirl generator. It was also seen, that a rotational speed of 920 rpm gives the best comparable results with LDV measurements, and that a rotational speed of 890 rpm gives almost zero torque on the runner, given that we don't have any frictional forces acting on the runner. Further investigation of the pressure oscillations were conducted, which at a rotational speed of 920 rpm revealed 3 distinct frequencies. One low frequency corresponding to an axial extraction/retraction of the vortex rope, one intermediate frequency corresponding to the rotation of the vortex rope, and one high frequency caused by the rotor stator interaction. Fourier analysis of the pressure history recorded at the wall of the draft tube showed that several new frequencies have been introduced compared to a previous study which was made on only the draft tube.

## 6 Future work

Future work for this case study could be to continue investigation of the SIMPLE based solver and try another turbulence models such as LES or DES. This could better predict the stagnation region seen for the meridional velocities in the draft tube. Since there has been alot of time spent on finding the "correct" rotational speed for this particular setup, one idea could be to customize a solver to adjust the rotational speed in accordance to the moment acting on the runner. This would make comparison with measurements alot easier as it would be easier to get the definite rotational speed corresponding to zero torque or if needed, any torque that is desired. This would also contribute to the OpenFOAM community.

## References

- [1] Open CFD. <http://www.openfoam.com>.
- [2] F. Avellan. Flow Investigation in a Francis Draft Tube: The FLINDT Project. In *Proceedings of the 20th IAHR Symposium on Hydraulic Machinery and Systems, Charlotte, USA. Paper DES-11*, 2000.
- [3] M. Beaudoin and H. Jasak. Development of a Generalized Grid Interface for Turbomachinery simulations with OpenFOAM. In *Proceedings of the OpenSource CFD International Conference, Berlin, Germany*, 2008.
- [4] A. Bosioc, S. Muntean, and R. Susan-Resiga. Numerical investigation of the jet control method for swirling flow with precessing vortex rope. In *Proceedings 3rd IAHR International Meeting of the Workgroup on Cavitation and Dynamic Problems in Hydraulic Machinery and Systems, Brno, Czech Republic*, October 14-16, 2009.
- [5] A. Bosioc, Susan-Resiga R., and S. Sebastian Muntean. Design and manufacturing of a convergent-divergent test section for swirling flow apparatus, 2008. National Center for Engineering of Systems with Complex Fluids, Polytechnica University of Timisoara, Timisoara, Romania.
- [6] A. Bosioc, C. Tanasa, S. Muntean, and R. Susan-Resiga. 2D LDV measurements and comparison with axisymmetric flow analysis of swirling flow in a simplified draft tube. In *Proceedings 3rd IAHR International Meeting of the Workgroup on Cavitation and Dynamic Problems in Hydraulic Machinery and Systems, Brno, Czech Republic*, October 14-16, 2009.
- [7] J. W. Cooley and J. W. Tukey. An algorithm for the machine computation of the complex fourier series. In *Mathematics of Computation*, pages Vol.19 , pp. 297–301, 1965.
- [8] Gerald B. Folland. *Fourier Analysis and its applications*. Brooks/Cole Publishing Company, 1992.
- [9] MathWorks Inc, 2010. <http://www.mathworks.com/access/helpdesk/help/techdoc/ref/fft.html>, april.
- [10] S. Muntean, R. Susan-Resiga, A. Bosioc, A. Stuparu, A. Baya, and L.E. Anton. Mitigation of Pressure Fluctuation in a Conical Diffuser with Precessing Vortex Rope Using Axial Jet Control Method. In *Proceedings of the 24rd IAHR Symposium on Hydraulic Machinery and Systems, Foz do Iguassu, Brazil*, 2008.
- [11] S. Muntean, R. Susan-Resiga, and H. Nilsson. 3d numerical analysis of the unsteady turbulent swirling flow in a conical diffuser using fluent and OpenFOAM. In *the 3rd IAHR International Meeting of the Workgroup on Cavitation and Dynamic Problems in Hydraulic Machinery and Systems, Brno, Czech Republic*. Brno University of Technology, October 14-16, 2009.
- [12] H Nilsson, M. Page, M. Beaudin, B. Gschaider, and H. Jasak. The OpenFOAM Turbomachinery Working Group, and Conclusions from the Turbomachinery Session of the Third OpenFOAM Workshop. In *Proceedings of the 24rd IAHR Symposium on Hydraulic Machinery and Systems, Foz do Iguassu, Brazil, Foz do Iguassu, October 27-31*, 2008.

- [13] O. Petit. Investigations of Incompressible Turbomachinery Applications using OpenFOAM, 2010. Thesis of licentiate of engineering, Department of Applied Mechanics, Chalmers University of Technology, Göteborg, Sweden.
- [14] R. Susan-Resiga and S. Muntean. Decelerated swirling flow in the discharge cone of Francis turbines. In *the 4th Symposium on Fluid Machinery and Fluid Engineering, Beijing, China*, November 24-27, 2008.
- [15] R. Susan-Resiga, S. Muntean, and A. Bosioc. Blade design for swirling flow generator, 2008. National Center for Engineering of Systems with Complex Fluids, Polytechnica University of Timisoara, Timisoara, Romaia.
- [16] R. Susan-Resiga, S. Muntean, C. Tanasa, and A. Bosioc. Hydrodynamic Design and Analysis of a Swirling Flow Generator, 2008. National Center for Engineering of Systems with Complex Fluids, Polytechnica University of Timisoara, Timisoara, Romaia.
- [17] R. Susan-Resiga, T.C Vu, S. Muntean, G.D Cicoan, and B. Nennemann. Jet Control of the Draft Tube Vortex rope in Francis Turbines at Partial Discharge. In *Proceedings of the 23rd IAHR Symposium on Hydraulic Machinery and Systems, Yokohama, Japan. Paper F192*, 2006.
- [18] H.K. Versteeg and W Malalasekera. *An Introduction to Computational Fluid Dynamics, The Finite Volume Method*. Pearson Education Limited, 2nd edition, 2007.